

Guided Electromagnetic Discharge Pulses Driven by Short Intense Laser Pulses: Characterisation and Modelling

M. Ehret,^{1,2} M. Bailly-Grandvaux,¹ Ph. Korneev,^{3,4} J.J. Apíñaniz,⁵ C. Brabetz,⁶ A. Morace,⁷ P. Bradford,⁸ E. d'Humières,¹ G. Schaumann,² V. Bagnoud,⁶ S. Malko,⁵ C. Matveevskii,³ M. Roth,² L. Volpe,⁵ N. C. Woolsey,⁸ and J.J. Santos¹

¹*Université de Bordeaux, CNRS, CEA, CELIA (Centre Lasers Intenses et Applications), UMR 5107, Talence, France*

²*Institut für Kernphysik, Technische Universität Darmstadt, Darmstadt, Germany*

³*National Research Nuclear University MEPhI, Moscow, Russian Federation*

⁴*P.N. Lebedev Physics Institute, Russian Academy of Sciences, Moscow, Russian Federation*

⁵*CLPU (Centro de Láseres Pulsados), Villamayor, Spain*

⁶*Plasma Physik/PHELIX, GSI Helmholtzzentrum für Schwerionenforschung GmbH, Darmstadt, Germany*

⁷*Institute of Laser Engineering (ILE), Osaka University, Osaka, Japan*

⁸*Department of Physics, York Plasma Institute, University of York, Heslington, UK*

(*M. Ehret currently at CLPU, Villamayor, Spain, mehret@clpu.es)

(Dated: September 2, 2022)

Strong electromagnetic pulses (EMP) are generated from intense laser interactions with solid-density targets, and can be guided by the target geometry, specifically through conductive connections to the ground. We present an experimental characterization, by time- and spatial-resolved proton deflectometry, of guided electromagnetic discharge pulses along wires including a coil, driven by 0.5 ps, 50 J, 10^{19} W/cm² laser pulses. Proton-deflectometry data allows to time-resolve first the EMP due to the laser-driven target charging and then the return EMP from the ground through the conductive target stalk. Both EMPs have a typical duration of tens of ps and correspond to currents in the kA-range with electric-field amplitudes of multiple GV/m. The sub-mm coil in the target rod creates lensing effects on probing protons, due to both magnetic- and electric-field contributions. This way, protons of 10 MeV-energy range are focused over cm-scale distances. Experimental results are supported by analytical modelling and high-resolution numerical particle-in-cell simulations, unraveling the likely presence of a surface plasma, which parameters define the discharge pulse dispersion in the non-linear propagation regime.

I. INTRODUCTION

Electromagnetic pulse (EMP) emission resulting from pulsed laser interaction with solid targets is reported for a large range of laser parameters with energies from 10 mJ to 1 MJ and intensities from 10^{14} W/cm² to 10^{20} W/cm² in the relativistic regime¹⁻⁶. In parallel, the guiding of such EMPs as an electrodynamic lensing technique is being pursued by groups interested in focusing and post-acceleration of laser-accelerated particle beams^{7,8}. Though these first particle-beam lensing experiments have considerably advanced our knowledge, the physical mechanisms responsible for the formation and propagation of guided EMP are not entirely understood. We present here experimental evidence of EMP bound to the target geometry and propose a model based on target discharge and geometry able to predict the EMP peak amplitude and dispersion relation. Furthermore, we follow the return current dynamics after the discharge pulse.

During laser interaction with a solid foil target a positive potential builds up close to the irradiated surface. This is due to laser-accelerated fast electrons that overcome the potential barrier and escape⁹. Electron charge extraction with ultra-intense (10^{18} W/cm² – 10^{20} W/cm²) sub-ps laser pulses ensues from mechanisms such Brunel-type resonance absorption^{10,11} and ponderomotive $j \times B$ acceleration^{12,13}. This gives rise to the generation of intense broadband EMPs propagating into the space surrounding the target, spectrally

ranging from radio frequencies¹⁴ to X-rays¹⁵.

Another fraction of electrons is accelerated forward into the target bulk. The most relativistic can leave the target at the rear side yielding a supplementary positive potential¹⁶. Potential created after both front- and rear side electron escape spreads along the target surface¹⁷, where according to particle-in-cell (PIC) simulations, a net non-zero charge density forms only within the skin depth¹.

This charge density does not spread neither instantly nor uniformly over the whole target body. The PIC simulations reveal a discharge wave with time-scale of tens of ps traveling along the target. In experiments with sub-ps laser driven wire targets, discharge pulses were observed several mm away from the laser-interaction region². These pulses show weak dispersion and attenuation during their linear propagation, but clear losses after reflection at the open end of a wire target. Modelling the pulse with a Sommerfeld wave^{2,18} reproduces qualitatively the observed strong radial electric- (E-) and azimuthal magnetic- (B-) field components. The long travel range with no considerable dispersion or attenuation was confirmed experimentally³.

The present investigation aims at the experimental characterization and physical understanding of the formation and evolution of such a discharge pulse and the subsequent return current dynamics. Particularly, we develop a new analytical model capable to describe and understand the observed propagation velocity and fine structure of the discharge pulses.

The model predictions are consistent with PIC simulations, where we can discriminate EMP in free space from target-bound EMP, and check the assumptions made for the modelling. We find that the positive potential evolves and gives rise to a pulsed electric current within the skin depth of the target rod, propagating with a group velocity close to the speed of light and bearing E- and B-fields. By using coil-shaped rods, the fields can be explored as lensing platforms for laser-accelerated beams of charges. We will consider here a simple scheme based on flat targets laser-cut from a thin metallic foil.

The paper is organized as follows, firstly experimental results are presented and a heuristic approach is applied to quantify the evolution of the target-bound discharge pulses. Secondly, PIC simulations are presented supporting the basic assumptions made for the heuristic analysis and allow further insights into the discharge pulse dynamics. Thirdly, an analytical approach to model the discharge pulse dispersion is presented, which agrees with the observed time-scales. The dynamics of pulsed return currents from the ground is explored in a fourth section. Finally, we conclude and comment on how EMP discharges can be used in future experimental applications.

II. EXPERIMENT

The experiment⁵ was carried out at GSI with the Petawatt High Energy Laser for Heavy Ion Experiments (PHELIX)¹⁹. We report on target discharges driven by laser pulses of 500 fs duration, 50 J energy and intensities of $5 \cdot 10^{18} \text{ W/cm}^2$. The targets are laser-cut in one piece from $50 \mu\text{m}$ thick flat Cu foils. All types of the four different targets comprise an interaction disk and a wire connection to the ground of $50^2 \mu\text{m}^2$ squared-section that includes a loop-feature of $250 \mu\text{m}$ -radius, as depicted in fig. 1: (a) Disk Loop Targets (DLT) with a helix-shaped loop, (b) Disk Ω -Coil Targets (DCT) and (c) Double-Plate Coil Targets (DPCT) with a Ω -shaped loop. DPCT have a more complex geometry with two parallel disks connected by the loop-shaped wire: the laser pulse passes through a hole in the front plate to drive the discharge from the rear plate. This geometry is simplified for a fourth target type: (d) DPCT-f has only the laser-irradiated plate, resulting in an open ended wire on one side of the loop. The interaction disks of DLT and DCT have a diameter of 2 mm, DPCT and their derivation DPCT-f have 3 mm diameter disks.

The discharge ps time- and mm spatial-scales were captured by proton-deflectometry. The probing proton particle beam is accelerated via Target Normal Sheath Acceleration (TNSA) using a second PHELIX laser beam portion similar to the discharge target driver, with an adjustable temporal delay. After crossing the target region of interest (ROI), the protons' deflections are imaged over a stack of Radiochromic Films (RCF), fig. 1 (e). Due to the characteristic Bragg peak of proton-energy absorption, each successive RCF image corresponds to the proton imprint of a small range of raising energy, therefore of different decreasing time-of-flight between the proton source and the ROI.

Deflectometry image data from a single shot are shown in

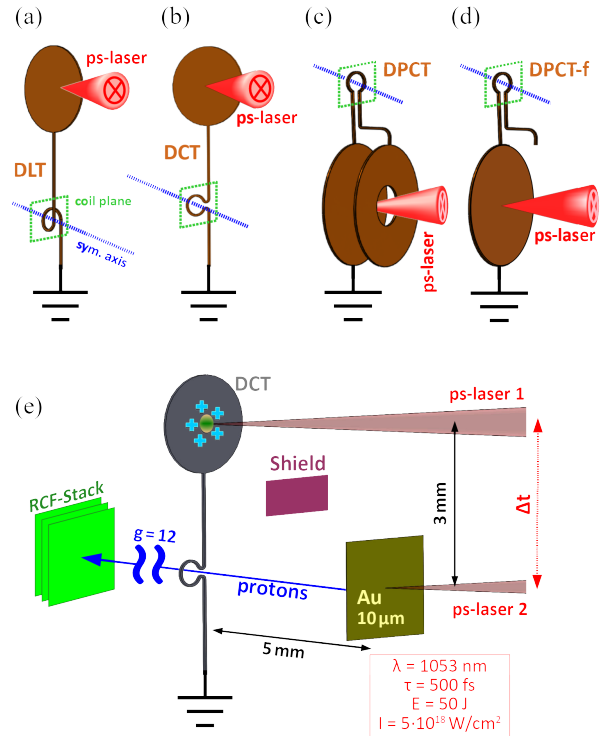


Figure 1: Targets are laser-cut in one piece from $50 \mu\text{m}$ -thick Cu foils. All types comprise an interaction disk and a loop of $250 \mu\text{m}$ -radius in their $50 \mu\text{m}$ -side squared grounding stalk: (a) Disk Loop Targets (DLT) with a helix-shaped loop, (b) Disk Ω -Coil Targets (DCT), (c) Double-Plate Coil Targets (DPCT) with a Ω -shaped loop and (d) Double-Plate Coil Targets without front plate (DPCT-f) with a Ω -shaped loop. (e) The set-up for target discharge and proton-deflectometry probing relies on two identical ps-laser pulses with adjustable delay Δt . ps-laser 1 induces a target discharge on the interaction disk and ps-laser 2 drives a proton beam from the rear surface of a $10 \mu\text{m}$ -thick Au foil. Deflectometry images are obtained from the proton dose deposition over a stack of RCF. A $100 \mu\text{m}$ -thick Tantalum shield blocks the direct line of sight between both laser interaction regions.

fig. 2 with a DCT. We obtained similar results with all target types, see fig. 3. The straight wire sections and the coil feature are clearly visible. For early times the target appears to be unaltered: deflections of protons then purely result from scattering in the solid density wire. Strong deflections away from the target rod with sharp caustics appear a few ps after target driving. After deflections reach their maximum, they decrease slowly back to zero, which conveys that they are not due to a thermally expanding target, but instead to a travelling EMP which wavefront propagation along the target wire is clearly evidenced through the image sequence.

For this very shot, given the chosen delay between the two laser pulses, 8.6 MeV and 9.3 MeV protons are those experiencing the peak amplitude of the propagating discharge pulse, as inferred from the larger horizontal deflections perpendicularly to the straight regions of the target rod. For both the

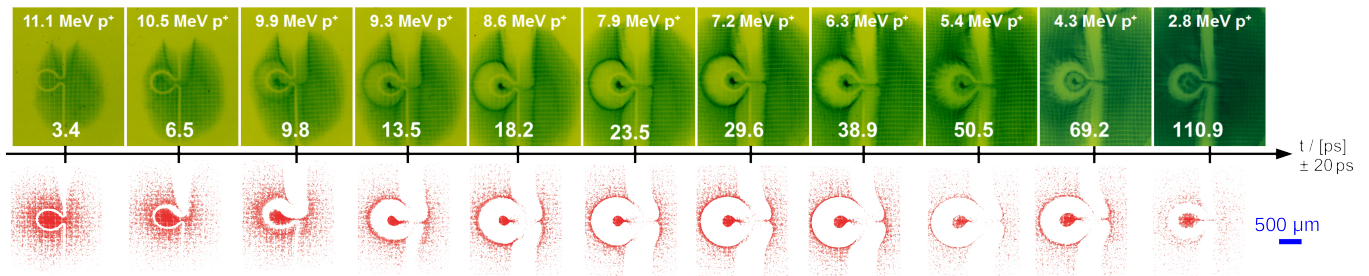


Figure 2: RCF proton imprints for different probing times within one shot using a DCT (top). Corresponding synthetic images (bottom) are obtained by coupled simulations of the dynamic target discharge pulse and test-particle probing. The laser pulse impacts the target disk above the field of view. The discharge pulse is coming from the top guided by the target geometry. The un-driven Ω -Coil (upper left RCF) has a diameter of $500\mu\text{m}$. All images have the same spatial scale indicated with a scale bar projected to the coil position. The witness mesh is positioned between proton source and coil - its periodicity projects to $106\mu\text{m}$ in the coil plane. For late times features like a ring-shaped caustic inside the coil and filaments are visible.

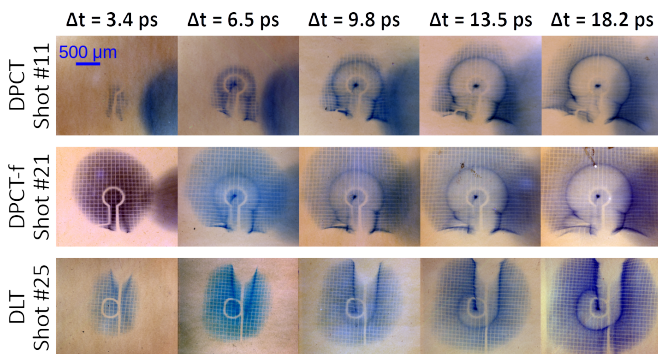


Figure 3: Proton deflectographs at distinct probing times for three shots using respectively a DPCT (top), DPCT-f (mid) and DLT (bottom). The discharge pulse comes from the laser interaction region and is guided by the target geometry. The initial diameter of the Ω -Coil is $500\mu\text{m}$ and all images have the same spatial scale, with the witness mesh having a periodicity of $106\mu\text{m}$ in the coil plane.

corresponding RCF layers, one observes an enhancement of the proton beam dose deposition in proximity of the loop's symmetry axis, interpreted as the result of focusing trajectories after crossing the loop region.

Though, in a non-stationary situation, when fields are changing rapidly for all positions of the proton path, the proton beam spectrum may change. The exact quantification of how much the emittance changes would require knowledge about the particle phase-space measured at three consecutive distances, which, for our setup, would only be achieved in three different shots assuming a perfect shot-to-shot reproducibility, to our best knowledge not yet feasible at high power laser facilities. To that, one would need to add identical reference shots without driving the coil targets. Despite these experimental limitations, we nevertheless propose a rough estimation of the transverse emittance perpendicular to the coil axis out of two distinct laser shots with the RCF stack placed at two different distances. We assume beam laminarity within narrow energy bins and beam focusing far be-

Table I: Group velocity of the wave front along straight sections of the Cu wire in units of the speed of light c . Laser parameters and target material were not intentionally varied.

Shot #25 allows observation of the wave front in two consecutive pairs of RCF, yielding two measurements that agree within the margins of their uncertainties.

Shot #	Discharge-Target Driver Energy	Target Type	Group Velocity v_g
11	51.5J	DPCT	$(0.77 \pm 0.10) \cdot c$
21	51.5J	DPCT-f	$(0.82 \pm 0.05) \cdot c$
22	47J	DCT	$(0.82 \pm 0.18) \cdot c$
37	53.5J	DCT	$(0.78 \pm 0.20) \cdot c$
41	41.4J	DCT	$(0.95^{+0.05}_{-0.10}) \cdot c$
25	44.3J	DLT	$(0.80 \pm 0.08) \cdot c$
25	44.3J	DLT	$(0.78 \pm 0.09) \cdot c$
39	51J	DLT	$(0.81^{+0.19}_{-0.25}) \cdot c$

hind the RCF stack. For these two shots the delay between the lasers was tuned to reach peak discharge amplitude at the probing time of 6.3 MeV protons. We observed that the transverse emittance of those protons passing through the loop is reduced by a factor ≈ 3 compared to reference shots without driving the coil: from initially $(1.59 \pm 0.05)\text{mm} \cdot \text{mrad}$ to $(0.5 \pm 0.1)\text{mm} \cdot \text{mrad}$. Note that changes of beam emittance can not arise with quasi-static electromagnetic lensing. Therefore, our results suggest longitudinal post-acceleration on timescales shorter than the transit time, changing the spectrum of the proton beam. These observations further highlight the non-stationary character of the guided discharges.

A. Evolution of the Discharge Pulse

Seven shots allowed to see the wave front propagation imprinted on consecutive RCF. The measured mean group velocity of the wave front along the Cu-target rod is $(0.82 \pm 0.06) \cdot c$, with the minimum value $(0.77 \pm 0.10) \cdot c$ and the maximum value $(0.95^{+0.05}_{-0.10}) \cdot c$. All measurements are given in table I.

The variation may be due to shot-to-shot differences in effective laser power and in target surface quality issuing from the laser cutting. The observed relativistic velocity close to that of light suggests the electromagnetic nature of the propagating wave, where electric and magnetic components are of a similar value.

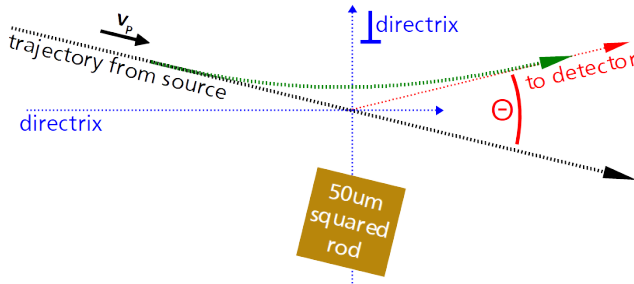


Figure 4: The geometry of the probing proton deflection around the target rod.

In order to reconstruct the discharge pulse amplitude versus time, we first deduce an approximation of a linear charge-density distribution $\lambda(\vec{x}, t)$ yielding the electric component of the discharge pulse. We assume that the E-field has a stronger influence than the B-field on radial (horizontal) deflections of probing protons along the straight target rod, for the accessed TNSA proton energy range of 1 – 20 MeV (well below relativistic values). The proton deflection angle $\Theta(\vec{x}, t)$, determined from the caustics imprinted on each RCF layer, is at maximum $\approx 3^\circ$. The deflection angle results of a radial acceleration with respect to the rod, as sketched in fig. 4. As first approximation, we neglect changes in the velocity component parallel to the directrix. Secondly, we set equal the norm of in- and outgoing velocity vector for trajectories from negative and positive infinity. In the limit of small deflection angles, we derive for the charge-density distribution:

$$\lambda \approx \frac{4\pi\epsilon_0}{q_p} \cdot \frac{m_p v_p^2}{2} \cdot \frac{\Theta}{\pi} \quad (1)$$

with m_p , q_p and v_p being the probing proton mass, charge and velocity respectively, and ϵ_0 the vacuum permittivity. With a deflection of 3° for protons of 10 MeV, we obtain $\lambda \approx 20$ nC/mm.

Accordingly, blue symbols in fig. 5 relate the temporal evolution of the radial deflections (quantified in units of raise in the proton energy component perpendicular to the probing axis; right-hand-side ordinates) with the deduced evolution of the charge distribution (left-hand-side ordinates). The temporal axis is given with respect to target drive, and individual measurements are compared using the respective proton arrival time at the Ω -coil. The peak of ≈ 25 nC/mm is reached at 10 ps and has a FWHM of ≈ 50 ps. We observe an exponential decay after the peak. We found a modified continuously differentiable Weibull function with purely exponential tail to fit the data, reading

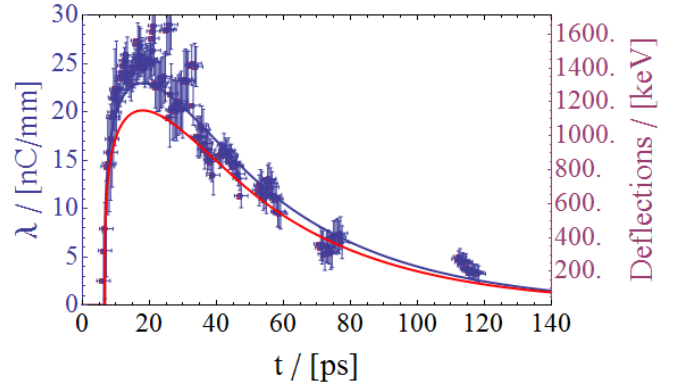


Figure 5: Evolution of the discharge pulse. Blue symbols yield values extracted upon electrostatic assumptions from deflectometry data in fig. 2 using eq. (1) around straight wire sections of a DCT. $t = 0$ ps corresponds to the driver laser impact on the target disk. For reference, proton probing times and measurement positions are converted to the respective arrival time of the discharge pulse at the Ω -Coil, assuming constant group velocity. The time uncertainty comprises the range of proton energies imprinted within one active RCF layer and the time the probing protons are in vicinity of the deflecting charge distribution, which is assumed to be of the order of the void around the wire. The gain of proton kinetic energy perpendicular to the probing axis is indicated on the plot's right hand side ordinate axis. A fit using eq. (2) (blue curve) yields an integrated charge of $Q_0 = (342 \pm 5)$ nC. Upon electrodynamic assumptions, data fits best to synthetic deflectograms when the former fit is renormalized to $Q_0 = 300$ nC (red curve).

$$f(x) = \frac{Q_0}{k + e - 1} \cdot \begin{cases} 0 & \text{if } x \leq 0 \\ \frac{k}{\sigma} \left(\frac{x}{\sigma}\right)^{k-1} \exp\left[1 - \left(\frac{x}{\sigma}\right)^k\right] & \text{if } 0 < x \leq \sigma \\ \frac{k}{\sigma} \exp\left[1 - \left(\frac{x}{\sigma}\right)^k\right] & \text{if } x > \sigma \end{cases} \quad (2)$$

where Q_0 denotes the normalization factor of the function representing the total target discharge and e is Euler's number. The parameters fit to $k = (1.25 \pm 0.02)$ and $\sigma = (10.1 \pm 0.3)$ mm. Integration of the fitting blue curve corresponds to an equivalent total target discharge of $Q_0 = (342 \pm 5)$ nC.

B. Dynamic Analysis

In order to reproduce synthetically the experimental RCF results, we performed dynamic test-particle transport and electromagnetic-field simulations with the Particle Field Interaction (PAFIN) code²⁰. The code processes any combination of magnetic- and electric fields with the possibility of defining current density and charge density distributions, and it allows implementation of analytical solutions for fields as

time-varying functions. After generation of a particle beam with a given phase space, either iterative step-wise transport or small angle projection of charged particles is coupled to a Lorentz force solver. For the particle-pushing calculations in this work, PAFIN was equipped with a structure-preserving second-order integration scheme²¹ suitable for relativistic particle motion in electromagnetic fields²².

In this simulation, the parameters of the EM-mode are derived from the measured group velocity and the fit of the discharge pulse: we solve the 1D continuity equation assuming a constant group velocity v_g ,

$$I(x, t) = v_g \cdot \lambda(x, t). \quad (3)$$

The discharge current $I(x, t)$ induces a B-field which co-propagates with the E-field. The temporal change of the fields are not explicitly taken into account for simplified simulations.

We perform dynamic simulations maintaining the fitted pulse shape, but re-normalizing it to different total charges Q_0 . We compare the best fitting simulation results, in the bottom row of fig. 2, to their exact experimental counterparts in the top row. Note the perfect agreement of asymmetric features of focused particles in the coil center for early probing times. Some small deviation of simulated deflectograms and experimental results are visible at the vicinity of the Ω -legs of the coil. We find $Q_0 = 300$ nC for the best overall agreement between experimental and synthetic deflectograms. The re-normalized peak (red curve) is compared to the original fit (blue curve) in fig. 5. Note that an earlier analysis of the discharge stream around the omega shaped part of the target rod²³ pointed out that a charge density on the wire alone, creating electrostatic fields, does not accurately reproduce the experimental proton-deflections.

Simulations indicate that the streaming EM-pulses have amplitudes of tens of GV/m and tens of T. Note that 10GV/m and 10T in SI units is ≈ 334000 statV/cm and 100000 G in Gaussian units. In order to understand the influence of such low amplitude B-field of several T comparatively to electrostatic effects on the probing protons of several MeV, we track the protons crossing the loop along the symmetry axis. We analytically estimate an upper limit for the deceleration prior to the target by equating the potential of an uniformly charged ring and the kinetic energy:

$$\Delta v_{\parallel \text{TNSA}} \leq 3\sqrt{\lambda_{\text{nC/mm}}} [\mu\text{m/ps}]. \quad (4)$$

Protons of several MeV kinetic energy have velocities of several $10 \mu\text{m/ps}$ – with $\lambda \approx 20$ nC/mm it leads to $\Delta v_{\parallel \text{TNSA}} \leq 13 \mu\text{m/ps}$. This relative change in velocity is non-negligible for the encountered field amplitudes. The electric component of the pulse is responsible for deceleration of particles prior to their transit through the coil - for one individual particle this ultimately results in a shorter length for focusing back to the axis by the effect of the magnetic lens corresponding to the loop current.

After transiting through the loop, the E-field would lead to a longitudinal re-acceleration. In the case of a static E-field, this would keep the in- and out-going kinetic energy of particles approximately equal. Yet, as the charge density evolution is asymmetric, the decelerating and accelerating potential vary. In simulations, the difference of particle energies before and after passing the coil is of the order of hundreds of keV.

Dynamic simulations also reproduce better imprints of the deflections around straight sections of the conductor rod. Access to the full phase space of the probing particles gives further insight in the dynamic processes at the vicinity of the conductor. Before transiting by the wire, the particle decelerates in the direction parallel to the directrix of the hyperbolic particle orbit. This violates the first assumption made to derive the charge density. For probing protons at 8.8 MeV, the change of kinetic energy reaches the order of 1 MeV.

In summary, when the Weibull fit to the discharge profile (blue curve in fig. 5) is fed into PAFIN proton tracing simulations, the proton deflections are larger than in the experimental data. This suggests the EM field amplitude has been over-estimated by eq. (1). After re-normalization of the discharge profile (red curve in fig. 5), however, we find that the PAFIN simulations agree very well with the experimental radiographs (see fig. 2).

C. Ambiguity of Results

Presuming the validity of the fit function eq. (2) with $\lambda(t) = f(v_g \cdot t)$, the EMP peak is attained after a rise time of

$$\tau_{\text{rise}} = \sqrt[k]{\frac{k-1}{k}} \cdot \frac{\sigma_{\text{exp}}}{v_g} \approx (11.3 \pm 1.2) \text{ ps} \gg \tau_L. \quad (5)$$

As seen in fig. 5, this rise time is about $22\times$ the laser pulse duration. This result may be a coupled effect of the target discharge in the *explosive* regime (as defined in ref. 24) on timescales longer than the laser drive and the temporal resolution of charged particle beam deflectometry in the low-MeV/u projectile energy range. We will refer to the charging dynamics later in this article.

The discharge pulse travels with a velocity of about $250 \mu\text{m/ps}$ which is approximately $5 - 25\times$ faster than the probing protons at $10 \mu\text{m/ps}$ for 1 MeV kinetic energy and up to $60 \mu\text{m/ps}$ for 20 MeV. Dynamic simulations show that the propagating EM-fields affect protons passing as far as approximately $250 \mu\text{m}$ distance from the wire. We see that the fastest protons are influenced by the discharge pulse for a duration corresponding to the rise time, as represented by the large uncertainty for the probing time in fig. 5. The pulse may have a shorter rise time with steep spatial gradients of the potential yielding three dimensional deflections that are not covered by the analysis according to eq. (1).

This ambiguity on the leading edge of the discharge pulse claims for further investigations with a better temporal resolution for the peak, e.g. by using short laser-pulse probing for future experiments based on electro- and magneto-optic ef-

fects in thin film crystals^{25,26}. This is beyond the scope of the present paper.

III. PIC SIMULATIONS

Our data analysis evidences pulsed electric and magnetic field components streaming along the target rod. For a deeper understanding of the nature of the discharge pulse, we performed 2D PIC simulations of the laser-target interaction using the PICLS code²⁷. The simulations resolve the successive propagation of electromagnetic waves and accelerated particle species. First, we performed five times down-scaled simulations (all sizes except the distance between the ends of the coil – legs of the Ω -shape) to capture the whole target geometry and distinguish the various transient electromagnetic effects: the propagation of fast electrons, EMP emission and guided discharge pulse. In a second step, real-scale 2D PIC simulations are used to study the generation of hot electron current and return current as well as associated electromagnetic fields.

The down-scaled simulations employ a driver laser pulse at the intensity of 10^{19} W/cm² comparable to the experiment but with $0.8\mu\text{m}$ wavelength and a pulse duration of 1.33 ps. The pulse interacts with the target in normal incidence with a $16\mu\text{m}$ FWHM focal spot. Its electric field oscillates in the simulation plane. The spatial and temporal profiles are flat top with Gaussian edges. The target plasma is composed of H ions and electrons with a initially uniform $10n_c$ density. The initial electronic and hydrogen temperatures are set to zero. The spatial step in both dimensions is 40 nm. The time step is 0.1 fs. The boundary conditions used are absorbing in both dimensions. Binary collisions and field ionization are not taken into account.

The resulting EM-energy-density $w_{em} = B_{\perp}^2/2\mu_0 + \epsilon_0 E_{\parallel}^2/2$ is given in fig. 6 (a – d,g) for different times. The driver laser pulse is injected at the left side of the simulation box. We see a discharge pulse bound to the target geometry at a high energy density, of several 10^{11} J/cm², and propagating at the velocity $0.964c$, close to that of light. Its spatially pulsed character is highlighted by a zoom in fig. 6 (g). The magnetic field amplitude perpendicular to the simulation plane is given for the same time (2.4ps) in fig. 6 (h). A spherical EMP in free space, that emanates from the interaction region with the velocity of light, is clearly distinguishable from the guided discharge pulse, which is slightly slower. For late times of 4.4ps, fig. 6 (f), we see strong magnetic fields in the vicinity of the laser-plasma interaction region. This indicates a return current building up.

The electron density 2.4ps after the interaction started is shown in fig. 6 (e) and zoomed in fig. 6 (i). Besides the plasma expansion in the hot interaction region, we identify a population of electrons that co-propagates with the discharge pulse.

The electric field streaming along the target has a monopole configuration in comparison to the fast oscillating EMP. The amplitude of the radial electric field at straight wire sections is 100GV/m in the simulation, scaling to 20GV/m in the experimental frame. The simulated amplitude of the magnetic field component around the target rod is 500T. This corresponds

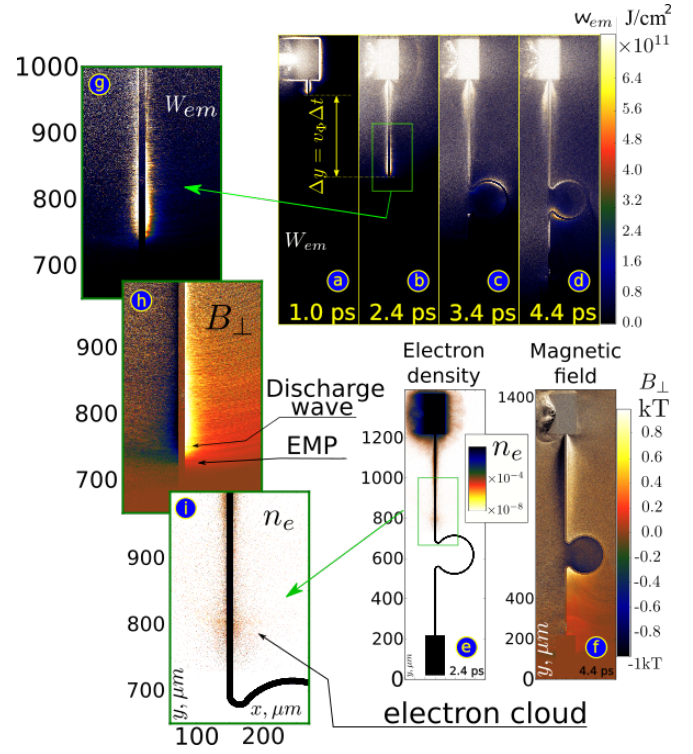


Figure 6: Down-scaled 2D PIC simulations of the laser driven discharge on DCT show target-bound discharge pulse, EMP in free space and an accelerated electron cloud following the discharge peak along the target wire. Panels (a – d,g) show the EM-energy-density in units of the 2D simulation, (f,h) the magnetic field strength perpendicular to the simulation plane and (e,i) the electron density. (g,h) highlight the spatially pulsed character of the discharge wave and (i) shows the accelerated electron cloud.

to 100T at the coil's center. Scaling to the experimental coil-size leads to ≈ 20 T at the coil center. Both components agree in field strength with the values heuristically deduced from experimental data in the previous section. The PIC simulations confirm a very strong radial electric field, and a weak azimuthal magnetic field. Around straight wire sections the electric field dominates the Lorentz force, in agreement with our initial assumption and supporting our evaluation of the guided EMP time evolution.

More detailed 2D PIC simulations are used to study the generation of hot electron current and return current as well as associated electromagnetic fields on real-scale $50\mu\text{m}$ thick foils. Here, we solely simulate the laser-target interaction region and a successive straight conductor section. The incident laser pulse with $1\mu\text{m}$ wavelength and a pulse duration of 100fs has a maximum intensity of 10^{19} W/cm² within the $3.5\mu\text{m}$ FWHM of the focal spot. The pulse interacts with the target in normal incidence. Its electric field is in the simulation plane. The spatial and temporal profiles are truncated Gaussians. The target plasma is composed of Al ions and electrons with a $700n_c$ maximum density. A $1\mu\text{m}$ longitudinal scale-length exponential pre-plasma is present in front of the

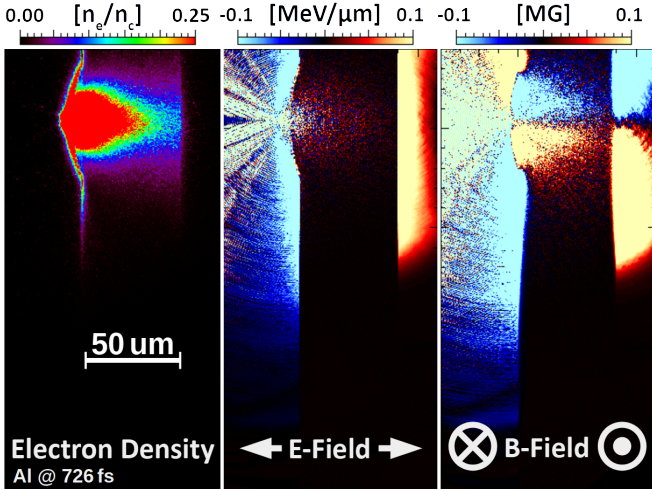


Figure 7: Real-scale 2D-PIC simulations showing the electron energy density, instantaneous E_x electric field, with horizontal axis x and instantaneous B_z magnetic field, with z the axis pointing out of the image plane, 726 fs after the beginning of the simulation.

target with a Gaussian transverse profile and a total length of $\Delta y = 10 \mu\text{m}$. The initial electronic and aluminum temperatures are set to zero. The spatial step in both dimensions is 20 nm and there are 2 Al ions and 26 electrons per cell. The time step is 0.066 fs. The boundary conditions used are absorbing in both dimensions. Field ionization using the ADK formula^{28,29} is taken into account as well as impact ionization. Binary collisions are also taken into account.

Instantaneous magnetic and electric fields as well as the electron density are shown in fig. 7, 726 fs after the beginning of the simulation. The laser pulse is injected at the left side of the simulation box. The maximum of the laser pulse enters the plasma after 330 fs. We observe an azimuthal magnetic field B_z of the order of 100 T appearing inside the target as well as in the vicinity of the target rod. Even though there are electrons down-streaming the target from the laser-interaction surface, the orientation of the surface magnetic field is clearly indicating a positive charge density propagation. The E_x electric field has a peak amplitude of several 100 GV/m.

The simulation reveals different EM waves originating from the interaction region along both surfaces of the target: a spherical EMP in free space is visible on the front side, propagating with the velocity of light. A discharge pulse propagates along front and rear target surfaces. The different progress can be explained by the delayed build up of the potential at the target rear side. From the time evolution of the B_z and E_x fields along the target surface, the velocity of the downward propagating EM mode on the front surface is measured to be 0.87c. This is in good agreement with the experimental values, regarding both Cu and Al as similar perfect conductors. We measure the rising edge of the amplitude of the B-field in vicinity of the conductor and divide it by the group velocity of the pulse: the rise time of (144 ± 48) fs is of the order of the driver laser pulse duration in the simulation.

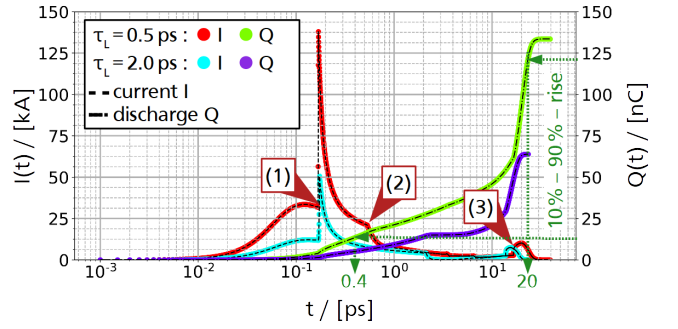


Figure 8: Evolution of the target discharge current I (red, cyan) and total charging Q (green, violet) simulated with ChoCoLaT2 at 50% absorption efficiency but two distinct pulse durations of 0.5 ps and 2 ps. Numbered labels indicate (1) the occurrence of the target rear side contribution to the current due to electrons that crossed the target, (2) the end of the laser pulse and (3) the time when, due to collisional cooling and ejection of most energetic electrons, the average Debye length of the hot electron distribution in the target becomes larger than the target thickness.

The dynamics of the guided EM pulse, with clear evidence of a spatial electromagnetic pulse with a mostly mono-mode transverse electric field structure, motivates analytical modelling efforts in order to conduct studies that do not require costly PIC simulations.

IV. MODELLING OF THE DISCHARGE PULSE

We will compare the experimentally deduced target charging with numerical simulations in a first part and a second part will be devoted to explore the discharge wave dispersion for a better understanding of the group velocity difference to the speed of light.

A first detailed attempt to model target charging in short laser pulse interactions^{24,30} allows to predict the expected discharge current due to laser-heated relativistic electrons. The numerical code ChoCoLaT2 simulates electron heating on a thin disk target and successive electron escape mitigated by the target potential, based on the driver laser parameters and the interaction geometry. It takes into account the collisions of electrons within cold solid density targets. The energy and time depending hot electron distribution function $f(E, t)$ evolves according to

$$\partial_t f(E, t) = \frac{h_L(E)\Theta(\tau_L - t)}{\tau_L} - \frac{f(E, t)}{\tau_{ee}(E)} - g(E, t) \quad (6)$$

where $h_L(E)$ is a constant exponential source of hot electrons, $\Theta(t)$ the Heaviside function limiting electron heating to the laser duration, $\tau_{ee}(E)$ the energy dependent cooling time and $g(E, t)$ the rate of electron ejection from the target. Source

term and normalization evaluate with

$$h_L(E) \stackrel{\dagger}{=} \frac{N_0}{T_0} \exp[-E/T_0] \quad (7)$$

$$N_0 \stackrel{\dagger}{=} \int f(E, 0) dE \quad (8)$$

The initial hot electron temperature T_0 depends on laser wavelength and pulse intensity^{12,31,32}; and N_0 is renormalized to the energy balance $N_0 T_0 = \eta E_L$ between the total energy of hot electrons in the target and the absorbed laser energy.

We perform ChoCoLaT2 simulations using our interaction parameters and a laser absorption between 30% and 50%. Resulting $Q_0 = (150 \pm 20)$ nC are of the same order of magnitude as the experimental value. Taking into account that ChoCoLaT2 systematically underestimates target charge by a factor of 2 to 3²⁴, we consider the agreement as fairly good.

A striking feature of the discharge wave propagation is its velocity different to the speed of light, with experimental data in table I. To understand this interesting phenomenon, consider the wire as a plasma cylinder with radius a , temperature T_e and electron density n_e . The electromagnetic wave propagation is considered using Maxwell equations in the cylindrical coordinate system (r, θ, z) with unit vectors $\vec{e}_r, \vec{e}_\theta, \vec{e}_z$, both inside and outside the plasma cylinder

$$\begin{cases} [\partial_z E_r(r, z, t) - \partial_r E_z(r, z, t)] \vec{e}_\theta = -\frac{1}{c} \partial_t \vec{B}(r, z, t), \\ \frac{1}{r} \partial_r [r B_\theta(r, z, t)] \vec{e}_z - \partial_z B_\theta(r, z, t) \vec{e}_r = \frac{1}{c} \partial_t \vec{D}(r, z, t), \\ \frac{1}{r} \partial_r [r D_r(r, z, t)] + \partial_z D_z(r, z, t) = 0. \end{cases} \quad (9)$$

Plasma properties are defined by the dielectric tensor, which non-zero components, in the simple case of Maxwellian collisionless plasma, read³³

$$\varepsilon_{rr}(\omega, k) = 1 - \frac{\omega_e^2}{\omega^2} F\left(\frac{\omega}{\sqrt{2}kv_T}\right), \quad (10)$$

$$\varepsilon_{zz}(\omega, k) = 1 + \frac{\omega_e^2}{(kv_T)^2} \left[1 + F\left(\frac{\omega}{\sqrt{2}kv_T}\right) \right], \quad (11)$$

where

$$F(x) = \frac{x}{\sqrt{\pi}} \lim_{\delta \rightarrow 0} \int_{-\infty}^{\infty} \frac{e^{-z^2}}{z - x - i\delta} dz, \quad (12)$$

and $\omega_e = \sqrt{4\pi n_e e^2 / m_e}$ is the electron plasma frequency, $v_T = \sqrt{T_e / m_e}$ is the thermal electron velocity, m_e is the electron mass.

To obtain the dispersion relation, the field components are transformed into their Fourier transform components,

$$\{E, B, D\}_i(r, z, t) = \int \{E, B, D\}_i(r, k, \omega) \cdot e^{-i(\omega t + kz)} dk d\omega, \quad (13)$$

and substituted to eq. (9), which provides a set of the second-order differential equations for cylindrical functions. The solutions should be finite at $r \rightarrow 0$ and $r \rightarrow \infty$, and also they must be joined at the edge of the plasma cylinder $r = a$. The consistency of all these conditions provides the dispersion relation

$$\frac{K_0(\alpha ka)}{K_1(\alpha ka)} = - \frac{\left(\frac{1}{\varepsilon_{rr}(\omega, k)} - \frac{\omega^2}{k^2 c^2} \right) I_0(\beta ka)}{\alpha \beta I_1(\beta ka)}, \quad (14)$$

where $\alpha \equiv \pm \sqrt{1 - \frac{\omega^2}{(kc)^2}}$, $\beta \equiv \pm \sqrt{\frac{\varepsilon_{zz}(\omega, k)}{\varepsilon_{rr}(\omega, k)} - \varepsilon_{zz} \frac{\omega^2}{(kc)^2}}$, $I_i(x)$ and $K_i(x)$ are i -th order modified Bessel functions of the first and the second kind respectively.

From the PIC simulations, we may conclude that the considered cylindrical plasma is hot and its initially sharp edges diffuse on the scale of the Debye length. It is possible to make only qualitative conclusions from the model dispersion eq. (14), using the effective electron plasma density of the hot layer around the original solid-density cold wire. According to the PIC simulations in fig. 6 the effective electron density is of the order of $n_e \sim 10^{18} \text{ cm}^{-3}$. Assuming the main frequency of the discharge wave to be of the order of the inverse laser pulse duration $\omega \sim 2\pi / \tau_L$, $\tau_L = 0.5$ ps, that is $\omega \approx 1.2 \times 10^{13} \text{ s}^{-1}$, we find that the plasma frequency for this effective electron density is somewhat higher $\omega_e \approx 5.6 \times 10^{13} \text{ s}^{-1}$. The difference between these two frequencies is an important parameter, which can explain an observed group velocity considerably lower than the light velocity. We can see in fig. 9 (a), for $n_e = 10^{18} \text{ cm}^{-3}$, that the group velocity is about 10% less than the light velocity in the domain $\omega \sim 10^{13} \text{ s}^{-1}$. This decrease is due to the decrease of the plasma frequency for low-density plasma close to the critical frequency for the propagating pulse.

Another important parameter in the model is the plasma temperature. It actually defines the rate of collisionless Landau damping, which is growing up with plasma temperature as more resonant particles are present in the system. In fig. 9 (a) three curves show the group velocity, numerically calculated from eq. (14) for three plasma temperatures. For a relatively low temperature $T_e = 1$ keV (red curve), the resonance at plasma frequency $\omega = \omega_e$ is very sharp, and the group velocity goes down quite deeply, to $\omega / (kc) \sim 0.6$. Increasing of the temperature results in smoothing of this discontinuity, as illustrated by the blue curve for $T_e = 50$ keV. For the parameters of the actual experiment, however, the scale of the hot electron energies in PIC simulations is about hundred keV. For this situation, the curve becomes very flat, decreasing at it most to $\omega / (kc) \sim 0.8 - 0.9$ (black curve), consistent with the experimental observation within error bars. Nevertheless, PIC simulations may overestimate the temperature, and lower temperatures can also explain the drop to values below 80% that were experimentally observed.

Note that comparing fig. 9 (a) and (b), the lower the electron density is, the lower is the group velocity for a given frequency. This result may have already been obtained, if one considers just the propagation of the wave along a cold copper wire³⁴. Thus, the highly nonlinear behavior of the group velocity is defined by the two main parameters; effective plasma

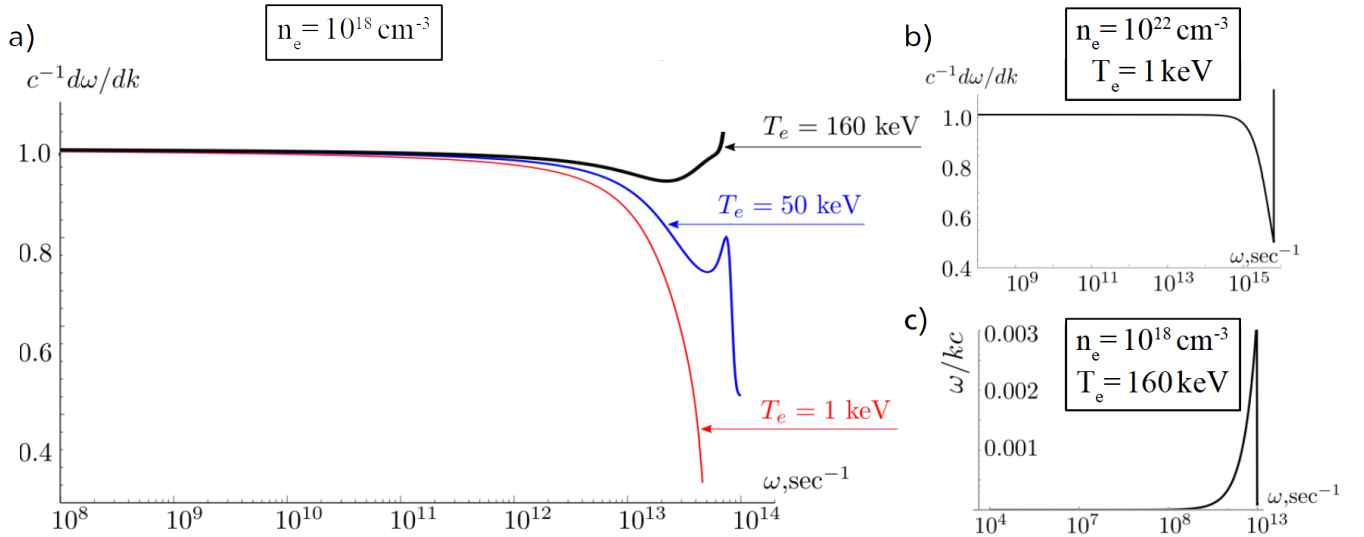


Figure 9: (a) Frequency dispersion of the discharge pulse group velocity, calculated numerically from the dispersion relation eq. (14), for $n_e = 10^{18} \text{ cm}^{-3}$ and $T_e = 1 \text{ keV}$ (red, lower curve), $T_e = 50 \text{ keV}$ (blue, middle curve), and $T_e = 160 \text{ keV}$ (black, upper curve). (b) shows the numerical solution for the group velocity for $n_e = 10^{22} \text{ cm}^{-3}$ and $T_e = 1 \text{ keV}$. (c) shows the phase velocity for the lower branch of the dispersion relation eq. (14) for $n_e = 10^{18} \text{ cm}^{-3}$ and $T_e = 160 \text{ keV}$.

density and temperature, both sensitive to the irradiation conditions. This may give rise to the variation of the experimentally observed values of the phase velocity, and motivates further experimental studies.

Landau damping is the only absorption mechanism, which makes the wave to be not purely transversal. This effect may contribute to effective electron acceleration along the wire^{35,36}, as seen in fig. 6 (i).

V. DYNAMICS AFTER THE DISCHARGE PULSE

Analysis of the proton-imprints in fig. 10 and fig. 11 allows to detail the evolution of the electromagnetic effects for later times. Following the full evolution for DPCT geometry in fig. 10 (a), the long tail of the discharge pulse continues to weakly squeeze the charged particle beam in proximity of the loop, but two striking changes arise: the appearance of a ‘sun-rayed’ pattern of caustics in vicinity of the coil and a doughnut shaped caustic inside the coil. Besides these two characteristic caustics, we diagnose the rise of the return current by the proton deflections around the coil, when probing perpendicularly to the coil axis (fig. 11).

A. Characteristic Caustics

A ‘sun-rayed’ pattern of proton density minima is visible on RCF imprints. It appears inside and around the coil and the stripes are perpendicular to the conductor surface. The perpendicularity is especially pronounced in the Ω -leg part for shot #32 with a DPCT, as shown in fig. 10 (b). Such caustics are observed in all shots, $(33 \pm 11) \text{ ps}$ after the passage of the pulse peak on the coil. The deflection pattern remains

stationary, caustics change contrast but not their location with respect to the conductor. The hydrodynamics of a wire plasma is too slow at the estimated heating rate to form a modulated plasma density at the observed distance around the wire. The observed ray-like structure is therefore probably defined by a modulation of the potential on the conductor or in direct vicinity of the target.

Variations in the potential might be caused by the rising return current, as studied in³⁷, Appendix D. That paper describes such fluctuations, without taking into account the retarded character of the evolving fields. Assuming a constant propagation speed of the pulse with $(0.82 \pm 0.06) \cdot c$ and a spread of retarded feedback with c , we obtain an estimated time-of-travel from interaction region to grounding and back to the coil of $(30.8 \pm 4) \text{ ps}$. Considering our target mounting with a conductive glue drop of $\approx 1 \text{ mm}$ diameter that holds the target on the grounding needle, time-of-travel and development of the caustic pattern overlap in the range of their uncertainty.

Another possible explanation for the ray pattern would be a modulation of the discharge wave itself. According to the model presented in the previous section for the discharge wave dispersion, the phase velocity of a short scale modulation of a Sommerfeld-like propagating wave appears to be very low. Accordingly, the ray-pattern would be almost constant during the observation time. In this case, consider a low-velocity branch of the solutions of eq. (14). In the limits $\omega \rightarrow 0$, $\omega/(kc) \rightarrow 0$, the dispersion relation gives to first order

$$(ka)^2 \left(\gamma + \ln \frac{2}{ka} \right) \pm 2 \left(\frac{kv_T}{\omega_e} \right)^2 \approx 0, \quad (15)$$

where $\gamma \approx 0.577$ is the Euler-Mascheroni constant. The constant value of the wave number $k \approx 1.12a^{-1}$, defined from

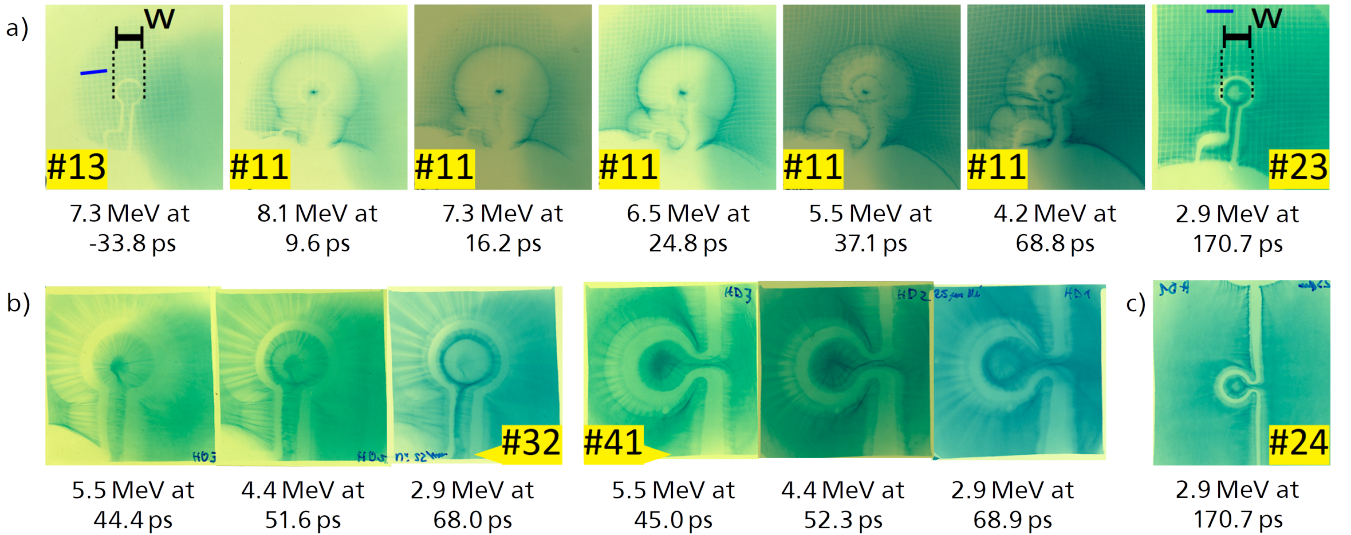


Figure 10: Typical evolution of deflections imaged on RCF for DPCT and DCT geometries. For DPCT in (a), the comparison of an early imprint (for shot #13) and a late imprint (for shot #23) with the magnification corrected scale-bar (w) as reference, we see that the coil rod increased by the order of two conductor widths, that is up to $100\ \mu\text{m}$. (b) For the exponentially decaying discharge pulse amplitude after passage of the peak at $\approx 12\ \text{ps}$, the intense imprint in the coil center issued from the dense beam progressively faints, while a ring shaped caustic appears, concentric with the coil. Both shots #32 and #41 in (b) were performed with increased magnifications by approaching the TNSA source to $1.99\ \text{mm}$ and $2.01\ \text{mm}$ from the coil plane respectively. DPCT deflectograms (shot #32) agree with the ones obtained for DCT geometry (shot #41), (c) also for latest probing times (shot #24). The center void within the ring shaped caustic lasts for our latest observations. Note the coil shadow in each imprint, the coil diameter is $500\ \mu\text{m}$ in the coil plane, blue bars in (a) indicate the distance of $6.5\ \text{mm}$ in the detector plane. The timing reference is the driver laser impact, proton energies are given, and probing times account for the time of flight from source foil to coil plane.

eq. (15), of the order of the inverse cylinder radius, corresponds to the low-velocity branch of the discharge wave. It may be excited if a seed perturbation, e.g. from the surface wire structure, is applied along the plasma cylinder. Comparing the spatial $\sim 50\ \mu\text{m}$ and temporal $\sim 30\ \text{ps}$ scales of the fine ray-like structure in fig. 10, we see, that this solution provides its qualitative description.

During the emergence of the ray-pattern, fig. 10 (b), the contrast of the beam on the coil axis becomes weaker, then progressively a ring-shaped sharp cusp appears with increasing contrast. The ring is concentric with the coil and clings close to the conductor on the inner side. For even later probing, no more protons reach the RCF on the coil axis and a clear void forms (see fig. 10 (c)). Void and ring are visible for the latest observation times, at $\approx 171\ \text{ps}$ after the laser-interaction. The ray pattern is barely visible already after $\approx 70\ \text{ps}$. The ring stays very clear. The evolution from focus point towards a strong ring-like deflection arises independently of the target geometry. Possibly, electrons coming from the laser interaction region get trapped in the vicinity of the coil and perturb proton deflectometry results.

After the passage of the full discharge wave, the proton image of the target appears nearly un-altered. Only for some shots, target rods are up to twice as large compared to images of the yet undriven target. The initially straight rod shows small surface modulations. Eventually ohmic heating³⁸ led to a slight expansion of the target wire with a velocity

of $\approx (0.5 \pm 0.3)\ \mu\text{m}/\text{ps}$, or we see deflections imposed by a slightly charged target with hundreds of pC/mm . Comparing an early imprint for shot #13 and a late imprint for shot #23 in fig. 10 (a) with the magnification corrected scale-bar (w), we see that the coil diameter slightly increased by the order of two conductor widths, that is $100\ \mu\text{m}$.

B. Magnetic Field Signature

Where early probing times, $< 60\ \text{ps}$, indicate B-fields induced by the displacement current of the discharge pulse, late probing times unravel a superposed charge-neutral return current. The magnetic field signature is more clearly evidenced in shots where the probe beam symmetry axis is set perpendicular to the axis of the omega-shaped coil (see fig. 11, where (a) and (b) correspond to DCT with the Ω -Coil or alternatively the Ω -legs facing the proton beam source, respectively). In such configurations, at earlier probing times, E-fields deflect symmetrically all protons passing above or below the coil's symmetry axis. With probing times greater than $60\ \text{ps}$, we start observing an asymmetry comparing both orientations. Such polarity in the deflection is a signature of B-fields, see fig. 11 (c). Bulb shaped caustics of this size are a widely observed phenomenon for ns-scale laser drive³⁹⁻⁴¹, and with the discussed target dimensions a clear indication of strong return currents.

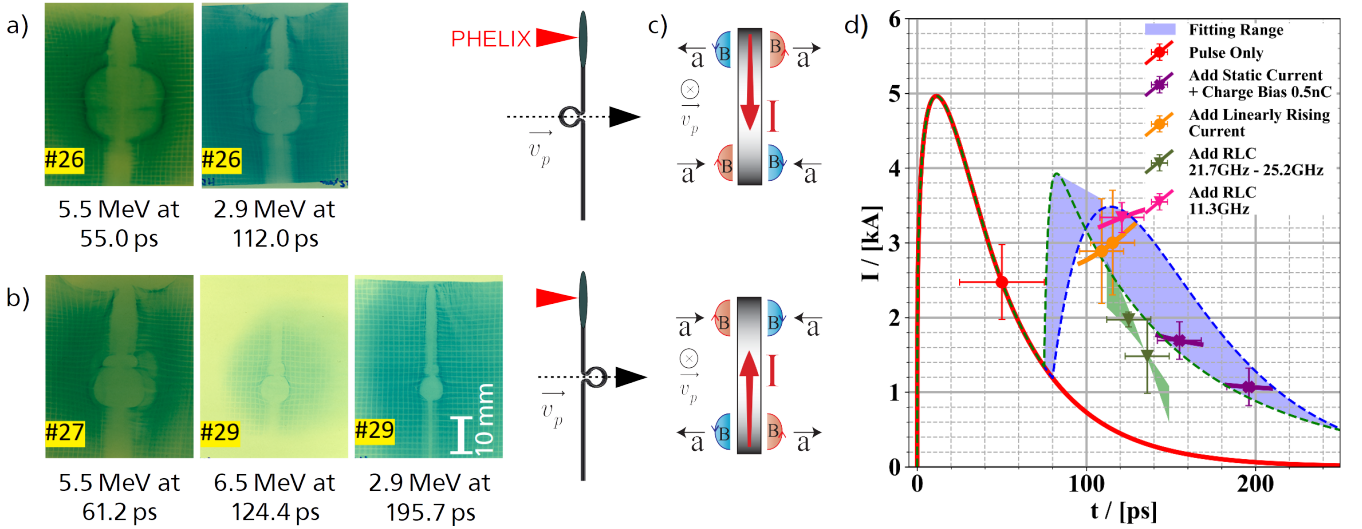


Figure 11: Current evolution based on RCF deflections for flat Ω -Coil Target geometry. Side-on deflectometry, where coil axis and probing axis are perpendicular, with (a) Ω -Coils and (b) Ω -legs facing the proton source side, yields a characteristic bulb shape due to the (c) differing Lorentz force in top- and bottom-sections of the coil (the direction of current is indicated for the side facing the source). Through (a–c) top and bottom rows show results of one versus the other orientation. The timing reference is the driver laser impact, proton energies are given. (d) Return current amplitudes are obtained by fitting data to dynamic synthetic deflectometry simulations. Early deflectographs can be reproduced with the discharge pulse alone (red curve and point), then a mismatch arises that can be resolved assuming static- (purple), linear- (orange) and sinusoidal currents (green and pink). Data points correspond to the best fitting amplitude within a temporal evolution plotted by a line or interval in the same color. The later temporal evolution is plotted for the time of the passage of the probing proton in vicinity of the coil. Fits to model eq. (17) yield a range of results plotted as 'fit range', probably based on shot-to-shot variations.

Note, that shot #27 in fig. 11 (b) witnesses a sudden change from symmetric to asymmetric deflections for probing at $t = 61.2\text{ps}$, a weak symmetric caustic is superposed by a strong asymmetric caustic. The field configuration may have changed rapidly during the passage of the probing particles.

The rise of a return current during the discharge wave decay is consistent with the target geometry. The discharge pulse reaches the grounding glue drop at $t = 24 \pm 4\text{ps}$, then spreads over a large area and drops in charge density, accordingly. Electrons from the target holder are eventually causing a return current to rise. This return current could reach the coil already at $t = 30.8 \pm 4\text{ps}$.

The bulb imprint on deflectograms does not change its polarity between passage of the discharge pulse and late times. This observation suggests there is a charge-neutral return current coming from the ground rather than a significant reflected charge pulse. There is no change in polarity during the full observation time of $\approx 200\text{ps}$.

Dynamic simulations with PAFIN reproduce the deflections for early times employing a linearly rising return current with $d_t I = 20\text{kA/ns}$. The simulations take into account the wave character of the current in the vicinity of the coil. Bulb sizes indicate currents of several kA, shown in fig. 11(d). Deflectograms of latest probing times at (150 – 200) ps can be well reproduced with the B-field of a quasi-static current in the target superposed to the E-field of a charge density bias on the wire that has the order of 0.5nC/mm . This order of magnitude for a residual charge density is consistent with the deflections

observed around straight sections of the target rod, discussed previously. Integrated over the full target surface, the total residual target charging is estimated to be $\approx 20\text{nC}$.

Linearly evolving or quasi-static return currents do not yield good agreement between experimental data and synthetic deflectograms for probing times of 100 ps to 140 ps, suggesting instead transient current dynamics. The return current I_{rc} forms due to the residual potential on the target. Assuming a lumped element RLC-circuit with the same current in the full wire part of the target, the governing equation is

$$\partial_t^2 I_{rc}(t) + 2\delta_{RL} \partial_t I_{rc}(t) + \omega_{LC}^2 I_{rc}(t) = 0. \quad (16)$$

with $\omega_{LC} = 1/\sqrt{LC}$ and $\delta_{RL} = R/(2L)$.

A flat copper DCT is modeled according to its geometry with a inductance of $L = 7.25\text{nH}$, a resistivity of $\eta = 16.8\text{n}\Omega\text{m}$ and a capacity of $C_1 = 222.5\text{fF}$. In the extreme case of an oxidized target consisting of CuO, assuming the same resistivity but at higher permittivity of $\epsilon_m = 18.1$, $C_2 = 1.28\text{pF}$.

Taking into account the skin depth⁴², one obtains $\omega_{RLC} = 25.15\text{GHz}$ and $\delta_{RL} = 34.43\text{MHz}$. For a fully oxidized CuO target one obtains instead $\omega_{RLC} = 5.91\text{GHz}$ and $\delta_{RL} = 16.96\text{MHz}$. For both cases, these numbers represent underdamped oscillations with $\omega_{LC} \gg \delta_{RL}$. The damping factor indicates a ns-scale current dynamics. Therefore we would expect an oscillation with frequency ω_{RLC} with periods ranging from $\approx 250\text{ps}$ to $\approx 1\text{ns}$ depending on the degree of oxidation. PAFIN simulations in this frequency range repro-

duce particular proton imprints in only some of all the shots, see fig. 11(d), but there is no possible fitting for all data points.

Instead, we observe a pulsed character of the current, which suggest the overdamped regime of the RLC system, $\omega_{LC} \ll \delta_{RL}$. Thus, a more accurate modeling is undertaken with the solution of a Pulse Discharge Current (PDC), with

$$I_{PDC}(t) = \frac{Q_0}{\alpha^{-1} - \beta^{-1}} \cdot (\exp[-\alpha t] - \exp[-\beta t])$$

$$\alpha = \delta_{RL} \pm \sqrt{\delta_{RL}^2 - \omega_{LC}^2}$$

$$\beta = 2\delta_{RL} - \alpha$$
(17)

The PDC model fits to the data in a wide range of parameters, as illustrated in fig. 11(d). The range where valid fit functions can be produced is indicated as the blue shaded area. The parameter α ranges from ≈ 25 GHz to ≈ 420 GHz and β then results inversely proportional with values from 25 GHz to 10 GHz. As the shape of the target visibly does not change with probing time, one may assume a constant inductance. With L , α and β set, the PDC model allows to calculate ranges for R and C , with

$$R = L \cdot (\alpha + \beta)$$

$$C = (L\alpha\beta)^{-1}.$$
(18)

The resistance ranges from 363Ω to 3118Ω and the capacitance from 220.7 fF to 32.84 fF, respectively. The latter suits well the capacity of a pure copper target, with a better agreement for the higher end of the interval. The corresponding resistance value of 363Ω indicates a resistance two orders of magnitude above the case of cold copper with $R \approx 5 \Omega$ for tens of GHz.

This increase of resistivity can be a further indication that the target is heated. A large increase in resistivity $\eta = m_e v_e(T_e) / q_e^2 n_e$ can be reasoned by the temperature depended electron collision frequency⁴³ and mutually low electron densities. For an electron density of $n_e = 10^{18} \text{ cm}^{-3}$ as seen in PIC simulations, and electron temperatures of 1 keV reasonable to explain the group velocity of the pulse (see fig. 9), the resistivity does increase to values that explain the large resistance, see fig. 12. An increase by the exact factor of 100 is calculated for a slightly lower temperature of 400 eV. Note that higher electron densities require lower temperatures to reproduce observations with our modelling for both the group velocity and the resistance.

Note further that surface plasma may change both the inductance and capacitance of the conductor. This underlines the importance of further studies aiming at experimental determination of the physical properties of the conductor.

VI. CONCLUSION

Our experiment has revealed pulsed kA-currents on the timescale of tens of ps dispersing on laser-driven discharge targets. The velocity and dispersion of prompt discharge

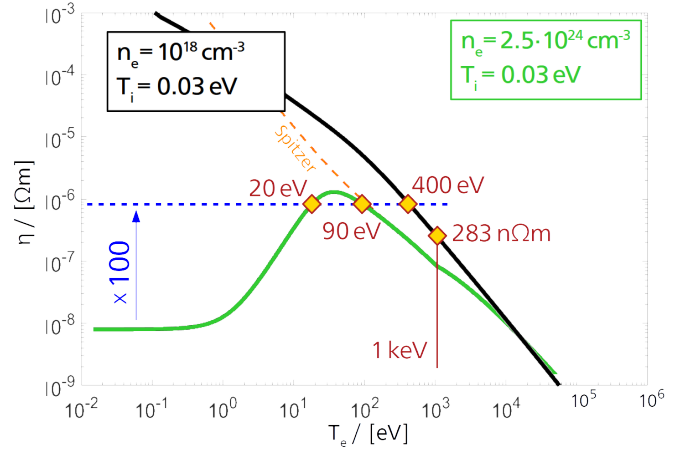


Figure 12: Resistivity calculated for Copper with cold background ions at different electronic densities. The green solid line illustrates the resistivity of solid density Copper, the dashed line indicates the Spitzer resistivity for this case. The black solid line depicts the Eidmann-Chimier resistivity for Copper at a density value discussed to explain the discharge wave dispersion.

pulses indicate that a hot surface plasma forms on the wire section that connects the target to ground.

We see that the temperature and electron density of the surface plasma are promising control parameters of the discharge pulse dispersion. The dispersion relation is responsible for a group velocity different from that of light. Solutions on the low branch of the dispersion relation agree with modulations of the target potential in their spatial dimensions and temporal growth rate. Even if for this experiment, the seed of the potential modulation is not being controlled, their imprint on the MeV protons is clearly visible. Further studies are necessary regarding the origin of the surface plasma, the discharge pulse dispersion relation and controlled seeding of potential modulations.

The laser-driven EM discharge pulse with amplitudes of tens of nC/mm and several kA precedes the return current in form of a pulsed discharge current with several kA. We, for the first time, experimentally separate both currents with a well defined Ω -loop shaped feature in the target rod. PIC simulations allow to distinguish EMP, fast electrons and a target-surface discharge wave propagation.

Building on this work, we see that relatively simple, flat metallic targets can be used for the chromatic lensing of charged particle beams. Using a dual laser set-up, energy-selection of the focused particles is possible by tuning the delay between the laser pulse driving the coil and the one generating the proton beam.

In the literature, comparable laser driven platforms are reported for the generation of pulsed magnetic fields⁴⁴, and the tailoring of laser-driven particle beams^{4,45}, but with no separation or identification of both transient currents. Note, that a parametric study of the discharge pulse parameters has been carried out recently⁴⁶, investigating charge density maximum and integral charge as a function of laser pulse duration, pulse

energy and pulse intensity. Higher magnetic fields may be expected in a similar, but a more compact setup, where the loop itself is irradiated at one of its ends and the discharge current is closed due to the expanding plasma⁴⁷. A partial characterization of the pulsed discharge current has been carried out in ref. 48, also demonstrating neutral kA currents. A detailed exploration of the discharge pulses discussed in this paper is important for a range of applications in laser physics and laser-driven charged particle beam acceleration, particularly for medical applications, the heating of material samples to warm dense matter conditions using ion beams and the fast ignition approach to fusion.

ACKNOWLEDGMENTS

We want to thank our funding projects POPRA Proj. 29910, IdEx U-BOR and CRA-ARIEL. PhK acknowledges support from the project # FSWU-2020-0035 Ministry of Science and Higher Education of the Russian Federation. This work was granted access to the HPC resources of CINES under the allocations 2016-056129 and 2017-056129 made by GENCI (Grand Equipement National de Calcul Intensif). The experimental work has been partially carried out within the framework of the EUROfusion Consortium and has received funding from the Euratom research and training program 2014-2018 and 2019-2020 under grant agreement No 633053. The views and opinions expressed herein do not necessarily reflect those of the European Commission.

REFERENCES

- ¹K. Quinn *et al.*, Phys. Rev. Lett. **102**, 194801 (2009).
- ²S. Tokita *et al.*, SR **5**:8268 (2015).
- ³H. Ahmed *et al.*, Phys. Rev. A **829** (2016).
- ⁴S. Kar *et al.*, Nat. Comm. **7**, 10792 (2016).
- ⁵M. Ehret *et al.*, “Energy selective focusing of TNSA beams by picosecond-laser driven ultra-fast EM fields,” News and Reports from HEDgeHOB **GSI-2017-2**, 19–20 (2017).
- ⁶F. Consoli *et al.*, High Power Laser Science and Engineering ,e22 (2020).
- ⁷S. Kar *et al.*, “Dynamic control of laser driven proton beams by exploiting self-generated, ultrashort electromagnetic pulses,” Physics of Plasmas **23**, 055711 (2016).
- ⁸M. Bardon *et al.*, “Physics of chromatic focusing, post-acceleration and bunching of laser-driven proton beams in helical coil targets,” Plasma Physics and Controlled Fusion (2020).
- ⁹A. Poyé *et al.*, Physical Review E **91**(4), arXiv:1503.02264v1 (2015).
- ¹⁰F. Brunel *et al.*, Phys. Rev. Lett. **59**, 52 (1987).
- ¹¹S.C. Wilks and W.L. Kruer, IEEE J. Quantum Electron. **33**, 1954 (1997).
- ¹²S. C. Wilks *et al.*, “Absorption of ultra-intense laser pulses,” Phys. Rev. Lett. **69**, 1383–1386 (1992).
- ¹³A. Pukhov and J. Meyer-ter-Vehn, Phys. Plasmas **5**, 1880 (1998).
- ¹⁴J.S. Perlman *et al.*, Appl. Phys. Lett. **31**, 414 (1977).
- ¹⁵C Courtois *et al.*, Phys. Plasmas **16**, 013105 (2009).
- ¹⁶M. Galletti *et al.*, “Direct observation of ultrafast electrons generated by high-intensity laser-matter interaction,” Appl. Phys. Lett. , 064102 (2020).
- ¹⁷S.P. Hatchett *et al.*, Phys. Plasmas **7**, 2076 (2000).
- ¹⁸A. V. Brantov, “Laser induced thz sommerfeld waves along metal wire,” EPJ Web of Conferences **195** (2018), DOI:10.1051/epjconf/201819503002.
- ¹⁹V. Bagnoud and F. Wagner, High Power Laser Science and Engineering **4**, e39 (2016).
- ²⁰M. Ehret, “Charged particle beam transport in intense electromagnetic fields,” Master Proposal Université de Bordeaux and Technische Universität Darmstadt (2015), DOI: 10.13140/RG.2.1.3820.0806.
- ²¹A. V. Higuera and J. R. Cary, “Structure-preserving second-order integration of relativistic charged particle trajectories in electromagnetic fields,” Physics of Plasmas **24**, 052104 (2017).
- ²²Note: Equation (19) in ref. 21 misses a factor of c^2 on the left hand side. Accordingly, we correct the last term in eq. (20) in ref. 21 to $\|\vec{\beta} \cdot \vec{u}\|^2 \cdot c^{-2}$ instead of $\|\vec{\beta} \cdot (\vec{u})^2\|$.
- ²³M. Ehret, “Tnsa-proton beam guidance with strong magnetic fields generated by coil targets,” Master Thesis Technische Universität Darmstadt (2016), DOI: 10.13140/RG.2.1.3855.7847.
- ²⁴A. Poyé *et al.*, Phys. Rev. E **98**, 033201 (2018).
- ²⁵I. Wilke *et al.*, “Single-shot electron-beam bunch length measurements,” Phys. Rev. Lett. **88**, 124801 (2002).
- ²⁶F. Bisesto *et al.*, “Novel single-shot diagnostics for electrons from laser-plasma interaction at sparclab,” Quantum Beam Sci. **1**, 13 (2017).
- ²⁷R. Mishra *et al.*, “Collisional particle-in-cell modeling for energy transport accompanied by atomic processes in dense plasmas,” Physics of Plasmas **20**, 072704 (2013).
- ²⁸A. M. Perelomov, V. S. Popov, and M. V. Terent’ev, “Ionization of atoms in an alternating electric field,” Sov. Phys. JETP, 924 – 934 (1966).
- ²⁹M.V. Ammosov, N.B Delone, and V.P. Krainov, “Tunnel ionization of complex atoms and of atomic ions in an alternating electromagnetic field,” Soviet Physics - JETP **64**(6), 1191–1194 (1986).
- ³⁰A. Poyé *et al.*, “Chocolat,” CELIA Program Library (2015), researchgate.net/publication/284609502_ChoCoLaT.
- ³¹R. Fabbro, C. Max, and E. Fabre, “Planar laser-driven ablation: Effect of inhibited electron thermal conduction,” The Physics of Fluids **28**, 1463–1481 (1985).
- ³²F. N. Beg *et al.*, “A study of picosecond laser-solid interactions up to e19wcm-2,” Physics of Plasmas **4**, 447–457 (1997).
- ³³E. M. Lifshitz and L. P. Pitaevskii, *Course of Theoretical Physics: Vol 10, Physical Kinetics* (Pergamon press, 1981).
- ³⁴V. Batygin and I. Toptygin, *Problems in electrodynamics* (Academic Press, 1964).
- ³⁵P. McKenna *et al.*, “Lateral electron transport in high-intensity laser-irradiated foils diagnosed by ion emission,” Phys. Rev. Lett. **98**, 145001 (2007).
- ³⁶A. S. Kuratov, A. V. Brantov, and V. Y. Bychenkov, “Modeling of laser generation and propagation of electron bunch along thin irradiated wire,” Bulletin of the Lebedev Physics Institute **45**, 346–349 (2018).
- ³⁷A. Poyé *et al.*, Physical Review E **92**(4-1), 043107 (2015).
- ³⁸V.T. Tikhonchuk *et al.*, “Quasistationary magnetic field generation with a laser-driven capacitor-coil assembly,” Phys. Rev. E **96**, 023202 (2017).
- ³⁹J.J. Santos *et al.*, New Journal of Physics **17**, 083051 (2015).
- ⁴⁰P. Bradford *et al.*, “Proton deflectometry of a capacitor coil target along two axes,” High Power Laser Science and Engineering **8**, e11 (2020).
- ⁴¹J. L. Peebles *et al.*, “Axial proton probing of magnetic and electric fields inside laser-driven coils,” Physics of Plasmas **27**, 063109 (2020).
- ⁴²W. C. Johnson, “Transmission lines and networks,” (McGraw-Hill, 1963) p. 58.
- ⁴³B. Chimier, V. T. Tikhonchuk, and L. Hallo, “Heating model for metals irradiated by a subpicosecond laser pulse,” Phys. Rev. B **75**, 195124 (2007).
- ⁴⁴B. Zhu *et al.*, “Ultrafast pulsed magnetic fields generated by a femtosecond laser,” Applied Physics Letters **113**, 072405 (2018).
- ⁴⁵H. Ahmed *et al.*, Scientific Reports **11**, 699 (2021).
- ⁴⁶E. Aktan *et al.*, “Parametric study of a high amplitude electromagnetic pulse driven by an intense laser,” Physics of Plasmas **26**, 070701 (2019).
- ⁴⁷I. V. Kochetkov *et al.*, “Neural network analysis of quasistationary magnetic fields in microcoils driven by short laser pulses,” Scientific Reports **12**, 13734 (2022).
- ⁴⁸W. W. Wang *et al.*, “Proton radiography of magnetic field produced by ultra-intense laser irradiating capacity-coil target,” (2014), arXiv:1411.5933.